

Fourier Transformers for Latent Crystallographic Diffusion and Generative Modeling

Jed A. Duersch^{1,2} **Elohan Veillon**^{1,2} **Astrid Klipfel**¹ **Adlane Sayede**² **Zied Bouraoui**¹

Abstract

The discovery of new crystalline materials calls for generative models that handle periodic boundary conditions, crystallographic symmetries, and physical constraints, while scaling to large and structurally diverse unit cells. We propose a reciprocal-space generative pipeline that represents crystals through a truncated Fourier transform of the species-resolved unit-cell density, rather than modeling atomic coordinates directly. This representation is periodicity-native, admits simple algebraic actions of space-group symmetries, and naturally supports variable atomic multiplicities during generation, addressing a common limitation of particle-based approaches. Using only nine Fourier basis functions per spatial dimension, our approach reconstructs unit cells containing up to 108 atoms per chemical species. We instantiate this pipeline with a transformer variational autoencoder over complex-valued Fourier coefficients, and a latent diffusion model that generates in the compressed latent space. We evaluate reconstruction and latent diffusion on the LeMaterial benchmark and compare unconditional generation against coordinate-based baselines in the small-cell regime (< 16 atoms per unit cell).

1. Introduction

The discovery of new crystalline materials underpins progress in energy storage, catalysis, and ionic transport. Useful phenomena may arise in compositionally rich and structurally complex unit cells containing many atoms and multiple chemical species (Mroz et al., 2022). Yet even for small unit cells, the size of the admissible design space scales rapidly with atom count and compositional diversity. Exhaustively exploring such high-dimensional design spaces using density functional theory (DFT) (Hohenberg &

Kohn, 1964; Kohn & Sham, 1965) is computationally costly, motivating the development of generative models that can propose physically plausible candidate structures at scale.

Recent generative models (e.g. (Zeni et al., 2025; Joshi et al., 2025; Levy et al., 2025)) can learn distributions over known crystals and propose new candidates for downstream screening, but extending these approaches to realistic crystallographic regimes remains challenging. Crystals are inherently periodic, with geometry defined on a three-dimensional torus and constrained by crystallographic symmetries (Klipfel et al., 2024; Rui et al., 2024), while many practically relevant materials exhibit variable atomic multiplicities and stoichiometries. Coordinate- and particle-based generators handle periodicity and symmetry through geometric conventions and equivariant architectures, but often incur substantial modeling overhead and, in many diffusion formulations, implicitly assume a fixed number of atoms. This limits support for generative moves that change multiplicity and complicates stable behavior across symmetry subgroups when composition changes.

In this work we take a different view: we represent each crystal through the truncated Fourier transform of a species-resolved unit-cell density, and perform learning and generation directly in reciprocal space. This representation is periodicity-native by construction and provides a compact, fixed-shape description that scales with unit-cell complexity. Importantly, crystallographic symmetries act on Fourier coefficients via simple algebraic transformations (permutations of wave vectors and phase shifts), turning symmetry structure into constraints on coefficients rather than geometric operations on particles. Because atomic multiplicity is encoded in the density, the representation also naturally supports variable numbers of atoms per species.

Building on this representation, we propose a two-stage reciprocal-space generative pipeline. We first train a transformer-based variational autoencoder (VAE) operating on complex-valued Fourier coefficients to learn a compact latent code that reconstructs lattice parameters, species information, and truncated Fourier content. We then train a latent diffusion model to generate in this latent space, enabling unconditional sampling followed by decoding and coordinate recovery. Our main contributions are:

¹CRIL UMR 8188, Université d'Artois, CNRS, France ²UCCS UMR 8181, Université d'Artois, France. Correspondence to: Jed A. Duersch <jalma.duersch@univ-artois.fr>.

(i) Reciprocal-space crystal representation and recovery: we introduce a truncated Fourier representation of species-resolved unit-cell density together with a practical recovery procedure that maps Fourier coefficients back to atomic configurations.

(ii) Complex-valued transformer VAE with latent diffusion generation: we built a transformer VAE for complex Fourier tokens and a latent diffusion model that performs generative sampling in the resulting compressed space.

(iii) Scalability and multiplicity support. With only nine Fourier basis functions per spatial dimension, our representation supports exact recovery for unit cells containing up to 108 atoms per chemical species and enables encoding and denoising of higher-count structures. In unconditional generation, latent diffusion amplifies the low-count skew present in the meta-stable dataset used for fine-tuning; accordingly, we focus quantitative generation comparisons on the *small-cell regime* (≤ 16 atoms per unit cell).

Our experiments validate recoverability from the truncated Fourier representation, stable VAE compression, and robust reverse diffusion in the signal-dominant regime. Unconditional sampling yields crystals with variable atom counts and symmetry-consistent fractional structure. These results establish the feasibility of reciprocal-space latent diffusion.

2. Related Work

Crystal representations for generative modeling A foundational choice in crystal generative modeling is the representation of atomic structure, which largely determines scalability and physical fidelity. Early approaches discretize unit cells into 3D voxel grids and model atomic or electron density as images using convolutional VAEs and GANs (Noh et al., 2019; Hoffmann et al., 2019; Court et al., 2020; Kim et al., 2020; Long et al., 2021; Kingma, 2013; Goodfellow et al., 2014), but these representations are memory-intensive and scale poorly with increasing unit-cell complexity. A second family of methods uses invertible, CIF- or POSCAR-inspired feature tensors to enable valid reconstruction and property conditioning (Ren et al., 2022; Bajpai et al., 2023; Zhu et al., 2024), at the cost of entangling composition, symmetry, and geometry in ways that can limit robustness under extrapolation. In these settings, periodicity, symmetry, and atom-count constraints are typically handled through explicit design choices (e.g., fixed grids, constrained parameterizations, or post-processing) rather than being made intrinsic to the primary modeling variables. Our work follows the density-field perspective (species-resolved unit-cell densities) but moves the primary modeling domain to reciprocal space via a truncated Fourier basis.

Diffusion models for crystal generation. Diffusion-based models have become a dominant paradigm for crystal gener-

ation due to their strong validity and stability. Most existing approaches operate directly in atomic coordinate space, diffusing positions, lattices, and sometimes atom types under geometric constraints (Tian et al., 2022; Luo et al., 2024; Jiao et al., 2024; Zeni et al., 2025), with subsequent work improving energetic fidelity and controllability through refined priors and conditional generation (Pakornchote et al., 2024; Ye et al., 2024; Xiaoshan et al., 2024; Mal et al., 2025). However, coordinate-space diffusion entails substantial geometric and combinatorial complexity, requiring explicit treatment of periodic boundaries, symmetry multiplicity, and typically assuming a fixed number of atoms. Latent-space diffusion can alleviate these issues by reducing dimensionality and accelerating sampling, but only if the latent representation has already factored out periodicity and symmetry-induced redundancies.

Symmetry-aware generative modeling A substantial body of work incorporates crystallographic symmetry explicitly into generative models. Wyckoff-position encodings and space-group constraints can improve validity (and sometimes sample efficiency) by restricting generation to symmetry-consistent degrees of freedom (Zhu et al., 2024; Sultanov et al., 2023; Rui et al., 2024; Levy et al., 2025; Kelvinius et al., 2025), but often trade generative flexibility for explicit control, require pre-specification of symmetry classes, or increase architectural and training complexity, especially when exploring under-characterized regions of crystal space or transitions between symmetry subgroups.

Transformer-based crystal generators Transformers are a natural backbone for crystal generation due to their ability to model long-range interactions and heterogeneous tokens. Autoregressive models such as CrystalFormer and WyFormer employ symmetry-constrained tokenizations informed by Wyckoff positions (Zhendong et al., 2024; Kazeev et al., 2025), while more recent diffusion-based transformer systems introduce hybrid discrete-continuous diffusion and property-guided generation pipelines (Takahara et al., 2024; Huang et al., 2024; Joshi et al., 2025; Yi et al., 2025). Despite these advances, transformer-based generators largely inherit the assumptions of their underlying encodings, motivating approaches that address scalability, symmetry, and compositional flexibility through the representation itself (and its latent compression), rather than relying only on architectural constraints.

Alternative paradigms Several alternative paradigms, including large language model-based encodings and Generative Flow Networks, have been explored (Nate et al., 2024; Xiao et al., 2023; Bengio et al., 2021; Hernandez-Garcia et al., 2023; Nguyen et al., 2023). These directions are complementary, but they typically focus on discrete interfaces, conditioning, or combinatorial search and therefore do not by themselves remove the representational redundancies.

dancy induced by periodicity and space-group structure that motivates our reciprocal-space approach.

3. Overview and Crystal representation

We propose a reciprocal-space generative pipeline for crystalline materials based on a truncated Fourier representation of the species-resolved unit-cell density. Instead of modeling atomic coordinates directly, we encode each crystal as (i) a rotation-invariant parametrization of the lattice and (ii) complex Fourier coefficients on a fixed reciprocal grid. This choice makes periodic boundary conditions exact by construction and exposes crystallographic symmetries as simple algebraic structure in the modeled variables.

Our pipeline has two stages. First, a **complex-valued transformer VAE** compresses the Fourier representation into a structured latent code and reconstructs lattice parameters, species information, and truncated Fourier coefficients. Second, a **latent diffusion model** generates these latent codes, enabling unconditional sampling followed by decoding and coordinate recovery. Because the zero-frequency Fourier coefficient encodes per-species multiplicity, the generator supports variable numbers of atoms per species without requiring a fixed-size point set during sampling.

3.1. Representation

A crystal is defined by a periodic arrangement of atoms in \mathbb{R}^3 . For our purposes, it is convenient to represent this structure by a unit cell whose contents are partitioned by atomic number. Let $\mathcal{Z} \subset \mathbb{Z}$ denote the set of atomic numbers present in the material. For each species $z \in \mathcal{Z}$, we define the corresponding subset of the unit cell by $\mathcal{U}_z = \{f_a^{(z)} \in [0, 1)^3 \mid a = 1, \dots, n_z\}$, where n_z is the number of atoms of species z , and fractional coordinates are taken in the half-open cube $[0, 1)^3$ to avoid boundary duplication. Repeating the unit cell over the integer lattice and embedding it in physical space using a lattice matrix $\mathbf{L} \in \mathbb{R}^{3 \times 3}$ yields the atomic positions

$$\mathcal{X}_z = \{\mathbf{L}(\mathbf{f} + \mathbf{k}) \mid \mathbf{f} \in \mathcal{U}_z, \mathbf{k} \in \mathbb{Z}^3\}.$$

The complete crystal configuration is the disjoint union over species present $\mathcal{X} = \bigsqcup_{z \in \mathcal{Z}} \mathcal{X}_z$.

Material properties are invariant under global rotations of the crystallographic axes. We therefore adopt a rotation-invariant and well-conditioned parametrization of lattice geometry using the matrix logarithm of its symmetric polar factor (Jiao et al., 2024). This yields an additive, rotation-invariant encoding of lattice shape that is stable across a wide range of length scales and well suited for learning and optimization. Full details are provided in Appendix B.1.

3.2. Truncated Fourier Transform of Atomic Density

One of the primary difficulties with diffusion models operating directly on atomic coordinates is the coherent handling of periodic boundary conditions. For example, nearest-neighbor computations require explicit replication across all 27 translations in $\{-1, 0, 1\}^3$, complicating graph-based or locality-sensitive architectures. Moreover, coordinate-wise diffusion does not naturally permit changes in atomic composition during the generative process. We instead construct a variational autoencoder that operates on the Fourier representation of species-resolved atomic density functions. This representation naturally enforces periodicity while allowing explicit control over the composition of each atomic species. Let $\mathcal{J} \subset \mathbb{Z}^3$ denote a truncated set of Fourier wave vectors,

$$\mathcal{J} = \{j \in \mathbb{Z}^3 \mid \|j\|_\infty \leq j_{\max}\}.$$

Each $j \in \mathcal{J}$ defines a Fourier basis function on the unit cube, $\varphi_j(\mathbf{f}) = \exp(2\pi i j^\top \mathbf{f})$. Representing each atom as a Dirac delta distribution, the Fourier coefficients of the atomic density for species z are given by

$$\alpha_j^{(z)} = \sum_{\mathbf{f} \in \mathcal{U}_z} \exp(-2\pi i j^\top \mathbf{f}), \quad j \in \mathcal{J}.$$

For each species, these coefficients combine to yield a vector $\alpha^{(z)} = [\alpha_j^{(z)}]_{j \in \mathcal{J}}$. The vectors are then assembled into a matrix representation of the full crystal,

$$\mathbf{A} = [\alpha^{(z_1)} \quad \alpha^{(z_2)} \quad \dots \quad \alpha^{(z_m)}].$$

Since the number of atoms in each species is contained in the α_0 coefficients, we easily know how many fractional coordinates to reconstruct from the Fourier coefficients.

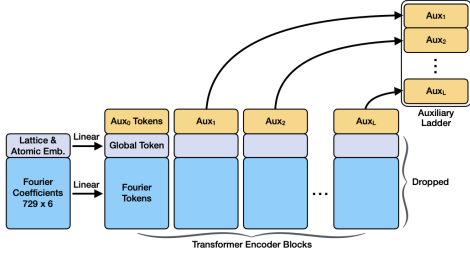
Symmetries and algebraic structure In Fourier space, crystallographic symmetries induce simple algebraic constraints among reciprocal-space coefficients. Specifically, a symmetry operation consisting of a lattice-preserving rotation \mathbf{M} and a fractional translation δ acts by permuting wave vectors and introducing phase shifts, yielding the relation

$$\alpha_j^{(z)} = \exp(-2\pi i j^\top \delta) \alpha_{\mathbf{M}^\top j}^{(z)}.$$

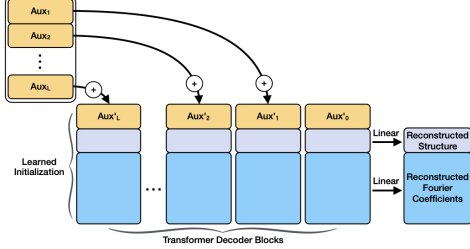
These structured relationships provide a natural mechanism for symmetry-aware compression and generation; full details are given in Appendix B.3.

4. Variational encoding and reverse diffusion

Our architecture combines a Perceiver-style bottleneck (Jaegle et al., 2021) with U-Net-style depth-aligned conditioning (Ronneberger et al., 2015) for reciprocal-space crystal representations. A small auxiliary token block interfaces with the large set of Fourier tokens: the encoder distills the full sequence into a depth-aligned auxiliary ladder, and the



(a) Encoder: L complex transformer blocks process auxiliary, global, and Fourier tokens. Auxiliary tokens are extracted at each depth and concatenated to form a depth-aligned auxiliary ladder.



(b) Decoder: tokens are reinitialized at the bottleneck. Depth-matched ladder slices are added to auxiliary tokens before each block to condition reconstruction.

Figure 1. Aux–Global–Fourier encoder–decoder with auxiliary ladder. The model separates tokens into a small auxiliary block, a single global structure token, and a large set of Fourier tokens. (a) The encoder distills information into a depth-aligned auxiliary ladder. (b) The decoder reconstructs structure and Fourier coefficients by injecting auxiliary ladder slices at matching depths.

decoder reconstructs from learned token initializations by injecting the corresponding ladder slices at each layer. This bottlenecked, depth-matched conditioning stabilizes reconstruction under strong compression. Figure 1 summarizes the encoder–decoder. The crystal input is embedded as a heterogeneous token sequence in a shared complex feature space (Appendix C.1).

Symmetry-aware latent compression In reciprocal space, crystallographic symmetries relate Fourier coefficients associated with rotated wave vectors, while translational symmetries appear as phase shifts. We do not explicitly enforce space-group constraints during training. Instead, we expose symmetry-relevant structure through (i) a fixed reciprocal-space grid in which each retained wave vector j is represented as a token, so that rotational symmetries act as permutations of tokens, and (ii) a Fourier-aware complex rotary positional encoding tied directly to j (Appendix D), which preserves relative phase structure. The auxiliary bottleneck encourages the model to compress global regularities, including symmetry-consistent correlations across wave vectors and species, into a compact latent code. We first train a VAE to reconstruct lattice parameters and Fourier coefficients, and subsequently train a latent diffusion model to sample these codes for unconditional generation.

4.1. Encoder–decoder architecture with auxiliary ladder

Each encoder and decoder layer is a complex-valued transformer block (RMSNorm, multi-head self-attention, gated MLP), implemented in complex space while remaining compatible with optimized real-valued attention kernels. Complex operations preserve phase throughout attention and residual streams, enabling rotary positional encodings tied to reciprocal-space wave vectors. In the baseline, the gated MLP modulates real and imaginary parts independently; Section 6.5 suggests a phase-preserving variant based on modulus gating can improve optimization efficiency without disrupting phase coherence. We use a Fourier-aware complex rotational encoding for positions; full details are in Appendix D. The VAE is a symmetric complex encoder–decoder that distills information into a compact auxiliary code and re-injects it during reconstruction (Fig. 1).

Encoder and auxiliary ladder construction The encoder consists of L stacked complex transformer blocks operating on the full token sequence, including auxiliary tokens, a single global structure token, and a large set of Fourier tokens. While all tokens participate in attention at each depth, only the auxiliary token block is retained after each transformer layer. Concretely, after the ℓ -th encoder block, the auxiliary token state $\text{Aux}_\ell \in \mathbb{C}^{n_{\text{aux}} \times d_{\text{model}}}$ is extracted and stored. Concatenating these states across depth yields a depth-aligned auxiliary ladder,

$$Z = [\text{Aux}_1; \text{Aux}_2; \dots; \text{Aux}_L],$$

which serves as the latent representation passed to the variational bottleneck. Fourier and global tokens act as contextual carriers during encoding but are not explicitly preserved. To encourage compact latent representations, auxiliary channels are progressively suppressed using a learned channel-wise mask trained under a signal-to-noise regularization scheme. This enables adaptive capacity allocation and permanent pruning of non-informative channels during training. Full details are provided in Appendix E.

Variational bottleneck The (masked) auxiliary ladder $\mu \in \mathbb{C}^{(L n_{\text{aux}}) \times d_{\text{model}}}$ parameterizes the mean of a diagonal complex Gaussian latent distribution. We associate each latent dimension with a learned real-valued log-scale σ and, using noise ε that is independent in real and imaginary components, sample the latent variable passed to the decoder as

$$Z = \mu + \varepsilon \odot \exp(\sigma), \quad \varepsilon \sim \mathcal{N}(0, I).$$

Decoder and depth-aligned conditioning The decoder mirrors the encoder with L complex transformer blocks but operates on a reinitialized token sequence. All tokens—auxiliary, global, and Fourier—are initialized from learned constants. At each decoder depth, a slice of the latent auxiliary ladder is injected additively into the auxiliary token block in depth-matched reverse order. Specifically,

before the i -th decoder block, the corresponding auxiliary slice is added only to the auxiliary tokens, while the remaining tokens are left unchanged. This auxiliary-only injection conditions the decoder on the encoded latent state without directly copying token content, allowing the decoder to reconstruct global structure and Fourier coefficients from scratch. After decoding, lightweight reconstruction heads map the decoded tokens to lattice parameters, species assignments, and Fourier coefficients. Details of the reconstruction heads and the multistage coordinate recovery procedure are provided in Appendix G.

4.2. Reverse diffusion in the auxiliary latent space

The role of this model is to denoise corrupted auxiliary ladders by predicting the injected noise, enabling iterative refinement in latent space.

Implementation The reverse diffuser is implemented as a complex-valued transformer with the same number of blocks as the encoder or decoder. Its input consists of a learned initialization tensor whose token dimension matches the size of the auxiliary ladder, augmented with additional scratch-pad tokens that are positionally encoded using the same Fourier-aware rotational scheme as the Fourier tokens. This learned initialization provides a nonzero baseline representation for all tokens. The noise-corrupted auxiliary ladder is added to the leading auxiliary portion of this initialization. This additive conditioning ensures that channels suppressed during encoding retain representational capacity during denoising and can participate in attention and intermediate computation. Several model components are conditioned on the diffusion coordinate using a lightweight quadratic interpolation scheme, enabling time-dependent modulation without introducing auxiliary networks. Full details are provided in Appendix H.

Selector-aware denoising To maintain consistency with the variational encoder, the reverse diffuser reuses the binary channel selector learned during encoding, applying denoising only to latent channels retained after auxiliary compression. This avoids imposing artificial constraints on the diffuser to reproduce exact zeros in pruned channels, which never encounter injected noise. After L transformer blocks, the diffuser outputs a noise estimate corresponding to the auxiliary ladder tokens, and training proceeds by comparing this prediction to the known injected noise under a standard diffusion objective.

5. Training Methodology

Training consists of two stages with coupled objectives: (i) training a variational autoencoder (VAE) to learn a compressible latent representation and reconstruct lattice/species/Fourier content, and (ii) training a reverse diffusion

model to denoise corrupted latent codes for generative sampling. To keep optimization stable across heterogeneous objectives, we normalize losses so that their effective gradient scales remain comparable: reconstruction terms are combined through a scale-invariant aggregation (Appendix F.1), and diffusion noise-prediction errors are normalized by per-channel noise scales (Appendix H.1). The encoder is shared between the VAE and diffusion stages. During VAE training, the encoder produces an auxiliary-ladder latent representation that is regularized to encourage compact, suppressible channels while maintaining reconstruction fidelity. During diffusion training, the encoder output serves as the target signal for a noise-conditioned denoising process operating directly in the auxiliary latent space.

5.1. Variational Auto-Encoder Training Objectives

The decoder predicts three components: lattice coefficients, species-slot assignments, and complex Fourier coefficients.

Species prediction Atomic numbers are predicted independently for each of up to six species slots using a cross-entropy loss over logits. An additional “empty” class accounts for unused slots.

Lattice reconstruction Lattice geometry is represented by six real-valued coefficients. Reconstruction error is measured using mean squared error (MSE), $\mathcal{L}_{\text{lat}} = \text{MSE}(\hat{s}, s)$.

Fourier reconstruction For each species slot, complex Fourier coefficients are reconstructed using the squared complex modulus, equivalently the sum of squared errors over real and imaginary components.

$$\mathcal{L}_{\text{four}} = \frac{1}{6|\mathcal{J}|} \sum_{z=0}^5 \left\| \hat{\alpha}^{(z)} - \alpha^{(z)} \right\|_2^2, \quad (1)$$

Scale-Invariant Reconstruction Aggregation Lattice and Fourier reconstruction losses are combined into a single reconstruction term $\mathcal{L}_{\text{rec}} = \sqrt{\mathcal{L}_{\text{lat}} + \mathcal{L}_{\text{four}}}$, forming a scale-invariant aggregation that maintains balanced gradient contributions across reconstruction terms throughout training. Details and motivation are provided in Appendix F.1.

Latent Signal-to-Noise Regularization Latent regularization is implemented using a signal-to-noise-based penalty that encourages compact, suppressible latent channels while avoiding the vanishing gradients associated with Gaussian KL regularization. Formal definitions and optimization rationale are given in Appendix E.2.

Full VAE Objective The training objective is

$$\mathcal{L}_{\text{VAE}} = \mathbb{E}_{\text{batch}} [\lambda_z \mathcal{L}_{\text{CE}}(\hat{z}, z) + \mathcal{L}_{\text{rec}} + \lambda_\mu \mathcal{L}_\mu], \quad (2)$$

where λ_z controls the contribution of species classification and λ_μ controls the strength of latent SNR regularization. The reconstruction term \mathcal{L}_{rec} has unit weight as a reference, with other terms weighted relative to it.

5.2. Reverse Diffusion Training

Latent Noise Model and Scale Estimation Reverse diffusion operates on noise-corrupted latent representations using a per-channel noise model with learned characteristic scales. The full noise distribution, moment matching, and scale estimation procedure are described in Appendix H.1.

Diffusion Schedule and Information-Matched Mixing

Latent variables are corrupted using a diffusion schedule designed to be approximately linear in expected information content, enabling stable training across signal- and noise-dominated regimes. The full schedule construction and parameterization are given in Appendix H.3.

Reverse Diffusion Objective Given (μ_ϕ, ϕ) , the reverse diffuser predicts the sampled noise $\hat{\eta}$. The training loss is the root-mean-squared error of the noise prediction, normalized by the decoder noise scale,

$$\mathcal{L}_\eta = \mathbb{E} \left[\|(\hat{\eta} - \eta)/\tau\|_2^2 \right]^{1/2}. \quad (3)$$

While signal reconstruction $\hat{\mu} = \frac{\mu_\phi - s_\phi \hat{\eta}}{c_\phi}$ is monitored during training, the signal error is not directly optimized.

Rationale for Noise Prediction Empirically, the most challenging regime for the reverse diffuser is the signal-dominant mixture, where s_ϕ is small and the noise contribution is weakly identifiable from μ_ϕ . In this regime, both noise prediction error and signal reconstruction error are largest. Optimizing a direct signal-reconstruction objective was found to be less stable and yielded inferior performance. The noise-prediction objective provides a well-conditioned regression target and naturally concentrates gradient pressure on the empirically limiting regime, without requiring additional schedule-dependent weighting. Combined with the information-matched diffusion schedule, this yields a robust and efficient reverse diffusion training procedure.

6. Experiments

6.1. Experimental protocol

LeMaterial provides a large, harmonized collection of crystalline structures aggregated from major repositories (Materials Project, Alexandria, OQMD), designed for large-scale ML in materials science (LeMaterial Consortium, 2025). We use the pre-filtered release containing approximately 2.8 million structures, most of which are DFT-relaxed local minima and therefore not guaranteed to be experimentally synthesizable. Many practically relevant candidates are *meta-stable*, i.e., near the formation-energy Pareto frontier for a given stoichiometry rather than at the global minimum. Filtering to meta-stable crystals yields 506,853 structures. Within this subset, 74.2% have at most 16 atoms per unit cell (the *small-cell regime*). We reserve 2048 meta-stable

Table 1. Head dimension sweep (vary D_{head} ; baseline $N_{\text{head}} = 12$, $N_{\text{layer}} = 8$). Width changes via $d_{\text{model}} = N_{\text{head}} D_{\text{head}}$. Best (lowest) values per column are bolded.

D_{head}	\mathcal{L}_{VAE}	$\mathcal{L}_{\text{four}}$	\mathcal{L}_{lat}	\mathcal{L}_μ	\mathcal{L}_{CE}
36	0.264	0.228	0.070	0.038	0.003
48	0.221	0.209	0.034	0.043	0.001
60	0.232	0.193	0.072	0.042	0.004

Table 2. Head count sweep (vary N_{head} ; baseline $D_{\text{head}} = 48$, $N_{\text{layer}} = 8$). Width changes via $d_{\text{model}} = N_{\text{head}} D_{\text{head}}$. Best (lowest) values per column are bolded.

N_{head}	\mathcal{L}_{VAE}	$\mathcal{L}_{\text{four}}$	\mathcal{L}_{lat}	\mathcal{L}_μ	\mathcal{L}_{CE}
10	0.216	0.186	0.061	0.045	0.001
11	0.229	0.195	0.069	0.039	0.001
12	0.221	0.209	0.034	0.043	0.001
14	0.269	0.236	0.072	0.033	0.001

structures for testing using a stratified split over unit-cell complexity, including 512 small-cell examples; all remaining meta-stable structures are used for fine-tuning.

Preprocessing and recoverability All crystals are preprocessed by converting species-resolved unit-cell densities to a truncated Fourier representation and snapping fractional coordinates to a rational grid to enable reliable inversion. We consider two regimes: (i) 7 basis functions per dimension ($7^3 = 343$ modes) with snapping to a 1/24 grid, and (ii) 9 basis functions per dimension ($9^3 = 729$ modes) with snapping to a 1/48 grid. On the full pre-filtered dataset, regime (i) flags 101,440 structures as unrecoverable, whereas regime (ii) flags only 27,005. Restricting to meta-stable subset, the corresponding counts are 40,793 versus 10,902. We therefore use $\text{bpd} = 9$ in experiments.

Training overview VAE is trained on the full preprocessed corpus (not only the meta-stable subset) to learn a broad reciprocal-space representation; encoding meta-stability directly in the latent space is non-trivial, so we impose this bias at generation time. The reverse diffuser is trained in two stages: pretraining on the full dataset to learn a general prior over latents, followed by fine-tuning on the meta-stable training split to steer sampling toward thermodynamically favorable structures. All experiments use a fixed data/model interface with maximum atomic number $z_{\text{max}} = 83$ and at most 6 chemical species per crystal. Unless otherwise noted, Fourier inputs use a cubic truncation with $\text{bpd} = 9$ basis functions per dimension and are evaluated on a $\text{gpd} = 48$ grid per dimension. We train with batch size 8 using Adam ($\beta_1 = 0.9$, $\beta_2 = 0.999$, $\epsilon = 10^{-8}$). The learning rate schedule consists of a linear warmup of 1000 steps from $\text{start_factor} \cdot \lambda$ to λ , followed by cosine annealing over $\text{anneal_steps} = 325,000$ steps down to $\lambda_{\text{min}} = 2 \times 10^{-5}$, with base learning rate $\lambda = 2 \times 10^{-4}$. All runs are trained for one epoch (approximately 333,727

Table 3. Depth sweep (vary N_{layer} ; baseline $D_{\text{head}} = 48$, $N_{\text{head}} = 12$). Best (lowest) values per column are bolded.

N_{layer}	\mathcal{L}_{VAE}	$\mathcal{L}_{\text{four}}$	\mathcal{L}_{lat}	\mathcal{L}_{μ}	\mathcal{L}_{CE}
7	0.238	0.218	0.052	0.040	0.001
8	0.221	0.209	0.034	0.043	0.001
9	0.218	0.189	0.063	0.038	0.001

Table 4. Reverse diffusion pretraining performance. All values are RMSE. Noise RMSE is the optimized training objective. Signal RMSE (diagnostic) is reported only for the signal-dominant bin and is normalized by the decoder noise scale. Lower is better.

Model	low- ϕ noise	mean noise	low- ϕ sig.
Baseline	5.063	2.734	0.603
$N_{\text{head}} = 10$	4.272	2.400	0.611

steps at batch size 8 for $\text{bpd} = 9$.

Baseline architecture Our baseline transformer VAE uses head dimension $D_{\text{head}} = 48$, $N_{\text{head}} = 12$ attention heads, and $N_{\text{layer}} = 8$ transformer blocks in both encoder and decoder. We parameterize model width as $d_{\text{model}} = N_{\text{head}} D_{\text{head}}$. Compression is controlled by a target nonzero-element budget factor $C = 8/12$ and a cosine schedule over nnz steps = 160k steps (details below).

6.2. Representation fidelity and recoverability

The truncated Fourier representation requires selecting a subset of retained wave vectors \mathcal{J} . While spherical truncation ($\|j\|_2 \leq j_{\text{max}}$) is analytically attractive for isolated atoms, we find it poorly matched to crystalline configurations, which often exhibit separable structure across coordinate directions. Across a large corpus of crystals, cubic truncation ($\|j\|_{\infty} \leq j_{\text{max}}$) consistently yields higher reconstruction success rates than spherical or hybrid truncations, even when the latter retain more basis functions.

Using cubic truncation, reconstruction success varies smoothly with atomic count and unit-cell occupancy. We observe successful reconstruction of unit cells containing up to 52 atoms of a single species using 7^3 retained modes ($j_{\text{max}} = 3$), and up to 108 atoms using 9^3 modes ($j_{\text{max}} = 4$). These trends are consistent with the recoverability statistics reported in Section 6.1, and further motivate the use of higher Fourier resolution when targeting structurally complex or high-occupancy unit cells.

6.3. VAE reconstruction performance

We perform coordinate-wise architectural sweeps over attention factorization ($D_{\text{head}}, N_{\text{head}}$), depth (N_{layer}), and auxiliary compression parameters. Only one hyperparameter is varied per sweep; Accordingly, the minima across Tables 1–8 need not correspond to a jointly optimal configuration. For

Table 5. Reverse diffusion fine-tuning on the meta-stable subset. Results are for a learning rate of 2×10^{-5} . Lower is better.

Model	low- ϕ noise	mean noise	low- ϕ sig.
Baseline	5.419	3.018	0.633
$N_{\text{head}} = 10$	4.674	2.661	0.604

Table 6. Path ablation over five architectural toggles. Each row corresponds to an 80k-step VAE training run following a structured enable/disable path. Reported losses are averages over the final 1200 steps. Consistently beneficial flips are bolded.

cyclic-slots	rms-bias	head-scale	mlp-bias	modulus-gating	\mathcal{L}_{VAE}
F	F	F	F	F	0.390
T	F	F	F	F	0.318
T	T	F	F	F	0.384
T	T	T	F	F	0.616
T	T	T	T	F	0.512
T	T	T	T	T	0.472
F	T	T	T	T	0.562
F	F	T	T	T	0.615
F	F	F	T	T	0.416
F	F	F	F	T	0.346

each configuration, we report results from seed achieving the lowest total objective \mathcal{L}_{VAE} for that configuration. \mathcal{L}_{VAE} is the total weighted training objective, decomposed into Fourier reconstruction loss $\mathcal{L}_{\text{four}}$, latent loss \mathcal{L}_{lat} , mean loss \mathcal{L}_{μ} , and element/species loss \mathcal{L}_{CE} . Across all configurations, the element/species cross-entropy loss \mathcal{L}_{CE} was consistently low and exhibited little sensitivity to architectural choices; we therefore treat it as non-limiting and do not use it to guide design decisions. Model width is parameterized as $d_{\text{model}} = N_{\text{head}} D_{\text{head}}$. The auxiliary ladder uses a cosine schedule on the number of nonzero elements (nnz), interpolating from a dense representation to a target nnz determined by the C factor over a specified number of steps.

Across sweeps, we observe a consistent tradeoff between Fourier reconstruction fidelity and latent regularization. While the best coordinate-wise configuration is close to the baseline, the head-count sweep in Table 2 indicates that reducing the number of attention heads can yield lower total VAE loss \mathcal{L}_{VAE} . Depth sweeps (Table 3) further suggest that additional layers may be beneficial, although these effects are not jointly optimized. Motivated by VAE performance, we compare both the baseline and the $N_{\text{head}} = 10$ architecture in subsequent reverse diffusion experiments.

6.4. Latent diffusion results

We evaluate reverse diffusion performance using the noise reconstruction root-mean-squared error (RMSE), which is the quantity directly optimized during training. During training, we partition results by the diffusion coordinate ϕ into five bins $\phi \in [0.01, 0.2], [0.2, 0.4], \dots, [0.8, 0.99]$. Reconstruction is most challenging in the signal-dominant bin ($\phi \in [0.01, 0.2]$). We additionally report the signal reconstruction RMSE as a diagnostic in this regime, which corresponds to one-shot signal reconstruction error, normalized by the decoder noise scale, and indicates whether the reconstructed signal lies within the range of corruption the decoder is trained to interpret.

Pretraining comparison Table 4 compares reverse diffusion pretraining performance between the baseline architecture and the $N_{\text{head}} = 10$ variant. The modified architecture substantially improves noise reconstruction in the signal-dominant regime, while also reducing the mean noise RMSE across the diffusion schedule. Signal reconstruction quality in the first bin remains comparable between architectures.

Meta-stable fine-tuning We fine-tune the reverse diffuser on the meta-stable subset. Performance is stable across learning rates spanning more than an order of magnitude; Table 5 reports the best values observed for each architecture. As in pretraining, $N_{\text{head}}=10$ architecture consistently achieves lower noise RMSE in the signal-dominant regime as well as lower mean noise RMSE. Signal reconstruction error in the first bin remains below the decoder noise scale, meaning the reconstructed signal is within the decoder’s operating regime. Full bin-wise results for fine-tuning across learning rates are in Appendix I.2. The results show that the modified architecture improves reverse diffusion performance where it is most challenging (when the noise component is small), while maintaining stable behavior across the full diffusion schedule and fine-tuning learning rates.

Unconditional generation 252,549 samples yielded 250,473 small-cell structures (≤ 16 atoms) and 2,076 medium-cell structures (17–32 atoms), with no larger unit cells observed. Since 74.2% of the meta-stable training set lies in the small-cell regime, this indicates amplification of dataset skew under unconditional diffusion, while still demonstrating support for variable atomic multiplicities.

6.5. Ablation study

To isolate the optimization impact of individual architectural components, we conduct a path-based ablation study over five binary design toggles. Rather than evaluating all 2^5 combinations, we follow a structured enable–disable path that incrementally adds components to a minimal configuration and then removes them in reverse order, capturing interaction effects while keeping the number of runs tractable.

All models are trained for 80k steps under identical settings. Performance is evaluated using the full VAE objective \mathcal{L}_{VAE} .

Overall, the ablation highlights the sensitivity of optimization to architectural biases and their interactions with the auxiliary ladder. Several components that were beneficial in earlier prototypes no longer improve performance in the current formulation; in particular, per-head output scaling consistently degrades optimization. In contrast, cyclic species-slot assignment yields the largest and most consistent improvement, while phase-preserving modulus gating provides a smaller but repeatable gain. Other effects appear interaction-dependent, requiring additional seeds to resolve.

7. Conclusion

We presented a reciprocal-space generative pipeline for crystalline materials based on a truncated Fourier representation of species-resolved unit-cell density. This encoding makes periodicity exact, exposes crystallographic symmetries as simple algebraic structure in reciprocal space, and avoids fixed-size point-set assumptions to enable variable atomic multiplicities during generation. We instantiate this representation with a complex-valued transformer VAE that compresses Fourier content into a structured auxiliary latent ladder, together with a latent reverse diffusion model that operates directly in this compressed space.

Empirically, we show that modest Fourier resolution supports exact coordinate recovery on rational grids for structurally complex, multi-species unit cells, and that reverse diffusion remains stable in the signal-dominant regime under appropriate architectural choices. While unconditional diffusion amplifies the small-cell regime present in the meta-stable training distribution, the encoder and diffuser remain capable of processing higher atom-count structures, indicating that conditioned or guided diffusion is a promising direction for extending generative coverage. Overall, these results position reciprocal-space modeling as a scalable alternative to coordinate-based crystal generators.

Impacts Statement This work advances generative modeling for crystalline materials by introducing a reciprocal-space formulation that natively handles periodicity and supports scalable latent diffusion. By enabling efficient modeling of structurally complex crystals, the proposed approach may accelerate computational materials discovery and screening workflows. The work is intended for scientific research applications and does not raise foreseeable negative societal impacts.

Acknowledgment

This work was supported by ANR-22-EXES-0009 MAIA and CNRS MITI interdisciplinary programs (PRIME AIM-

GPT), and was granted access to the HPC resources of IDRIS under the allocation made by GENCI.

References

Aroyo, M. I. International tables for crystallography, Space-Group symmetry, 2017.

Bajpai, R., Shukla, A., Kumar, J., and Tewari, A. A scalable crystal representation for reverse engineering of novel inorganic materials using deep generative models. *Computational Materials Science*, 230:112525, 2023.

Bengio, E., Jain, M., Korablyov, M., Precup, D., and Bengio, Y. Flow network based generative models for non-iterative diverse candidate generation. *Advances in Neural Information Processing Systems*, 34:27381–27394, 2021.

Court, C. J., Yildirim, B., Jain, A., and Cole, J. M. 3-d inorganic crystal structure generation and property prediction via representation learning. *Journal of Chemical Information and Modeling*, 60(10):4518–4535, 2020.

Eilers, F. and Jiang, X. Building blocks for a complex-valued transformer architecture. *ArXiv*, abs/2306.09827, 2023. URL <https://arxiv.org/abs/2306.09827>.

Goodfellow, I., Pouget-Abadie, J., Mirza, M., Xu, B., Warde-Farley, D., Ozair, S., Courville, A., and Bengio, Y. Generative adversarial nets. *NeurIPS*, 27, 2014.

Hernandez-Garcia, A., Duval, A., Volokhova, A., Bengio, Y., Sharma, D., Carrier, P. L., Kozlarski, M., and Schmidt, V. Crystal-gfn: sampling crystals with desirable properties and constraints. *Proceedings of NeurIPS 2023*, 2023.

Hoffmann, J., Maestrati, L., Sawada, Y., Tang, J., Sellier, J. M., and Bengio, Y. Data-driven approach to encoding and decoding 3-d crystal structures. *arXiv:1909.00949*, 2019.

Hohenberg, P. and Kohn, W. Inhomogeneous electron gas. *Physical review*, 136(3B):B864, 1964.

Huang, C., Chen, J., Chen, C., Chen, C., Su, R., Du, S., Liang, H., Lin, D., et al. A generation framework with strict constraints for crystal materials design. *arXiv preprint arXiv:2411.08464*, 2024.

Jaegle, A., Gimeno, F., Brock, A., Vinyals, O., Zisserman, A., and Carreira, J. Perceiver: General perception with iterative attention. In *International conference on machine learning*, pp. 4651–4664. PMLR, 2021.

Jain, A., Ong, S. P., Hautier, G., Chen, W., Richards, W. D., Dacek, S., Cholia, S., Gunter, D., Skinner, D., Ceder, G., and Persson, K. A. Commentary: The materials project: A materials genome approach to accelerating materials innovation. *APL Materials*, 1(1):011002, 07 2013. ISSN 2166-532X. doi: 10.1063/1.4812323. URL <https://doi.org/10.1063/1.4812323>.

Jiao, R., Huang, W., Lin, P., Han, J., Chen, P., Lu, Y., and Liu, Y. Crystal structure prediction by joint equivariant diffusion. *NeurIPS*, 36, 2024.

Joshi, C. K., Fu, X., Liao, Y.-L., Gharakhanyan, V., Miller, B. K., Sriram, A., and Ulissi, Z. W. All-atom diffusion transformers: Unified generative modelling of molecules and materials. *arXiv preprint arXiv:2503.03965*, 2025.

Kazeev, N., Nong, W., Romanov, I., Zhu, R., Ustyuzhanin, A., Yamazaki, S., and Hippalgaonkar, K. Wyckoff transformer: Generation of symmetric crystals. *arXiv preprint arXiv:2503.02407*, 2025.

Kelvinius, F. E., Andersson, O. B., Parackal, A. S., Qian, D., Armiento, R., and Lindsten, F. Wyckoffdiff—a generative diffusion model for crystal symmetry. *arXiv preprint arXiv:2502.06485*, 2025.

Kim, B., Lee, S., and Kim, J. Inverse design of porous materials using artificial neural networks. *Science advances*, 6(1):eaax9324, 2020.

Kingma, D. P. Auto-encoding variational bayes. *arXiv preprint arXiv:1312.6114*, 2013.

Klipfel, A., Bouraoui, Z., Peltre, O., Fregier, Y., Harrati, N., and Sayede, A. Equivariant message passing neural network for crystal material discovery. In *Proceedings of the AAAI Conference on Artificial Intelligence*, volume 37, pp. 14304–14311, 2023.

Klipfel, A., Fregier, Y., Sayede, A., and Bouraoui, Z. Vector field oriented diffusion model for crystal material generation. In *Proceedings of the AAAI Conference on Artificial Intelligence*, volume 38, pp. 22193–22201, 2024.

Kohn, W. and Sham, L. J. Self-consistent equations including exchange and correlation effects. *Physical review*, 140(4A):A1133, 1965.

LeMaterial Consortium. Lematerial: Large-scale materials datasets for machine learning. <https://huggingface.co/datasets/LeMaterial>, 2025. <https://huggingface.co/datasets/LeMaterial/LeMat-Bulk>.

Levy, D., Panigrahi, S. S., Kaba, S.-O., Zhu, Q., Lee, K. L. K., Galkin, M., Miret, S., and Ravanbakhsh, S. Symmcld: Symmetry-preserving crystal generation with

diffusion models. *arXiv preprint arXiv:2502.03638*, 2025.

Long, T., Fortunato, N. M., Opahle, I., Zhang, Y., Samathrakis, I., Shen, C., Gutfleisch, O., and Zhang, H. Constrained crystals deep convolutional generative adversarial network for the inverse design of crystal structures. *npj Computational Materials*, 7(1):66, 2021.

Luo, Y., Liu, C., and Ji, S. Towards symmetry-aware generation of periodic materials. *Advances in Neural Information Processing Systems*, 36, 2024.

Mal, S., Mishra, S., and Sen, P. Diffcrysge: A score-based diffusion model for design of diverse inorganic crystalline materials. *arXiv preprint arXiv:2505.07442*, 2025.

Mroz, A. M., Posligua, V., Tarzia, A., Wolpert, E. H., and Jelfs, K. E. Into the unknown: How computation can help explore uncharted material space. *Journal of the American Chemical Society*, 144(41):18730–18743, Oct 2022. ISSN 0002-7863. doi: 10.1021/jacs.2c06833. URL <https://doi.org/10.1021/jacs.2c06833>.

Nate, G., Anuroop, S., Andrea, M., Andrew, G. W., C. Lawrence, Z., and Zachary, U. Fine-tuned language models generate stable inorganic materials as text. *arXiv:2402.04379*, 2024.

Nguyen, T. M., Tawfik, S. A., Tran, T., Gupta, S., Rana, S., and Venkatesh, S. Hierarchical gflownet for crystal structure generation. In *AI for Accelerated Materials Design-NeurIPS 2023 Workshop*, 2023.

Noh, J., Kim, J., Stein, H. S., Sanchez-Lengeling, B., Gre-goire, J. M., Aspuru-Guzik, A., and Jung, Y. Inverse design of solid-state materials via a continuous representation. *Matter*, 1(5):1370–1384, 2019.

Pakornchote, T., Choomphon-Anomakhun, N., Arrerut, S., Atthapak, C., Khamkaeo, S., Chotibut, T., and Bovornratanaraks, T. Diffusion probabilistic models enhance variational autoencoder for crystal structure generative modeling. *Scientific Reports*, 14(1):1275, 2024.

Perdew, J. P., Burke, K., and Ernzerhof, M. Generalized gradient approximation made simple. *Physical review letters*, 77(18):3865, 1996.

Ren, Z., Tian, S. I. P., Noh, J., Oviedo, F., Xing, G., Li, J., Liang, Q., Zhu, R., Aberle, A. G., Sun, S., et al. An invertible crystallographic representation for general inverse design of inorganic crystals with targeted properties. *Matter*, 5(1):314–335, 2022.

Ronneberger, O., Fischer, P., and Brox, T. U-net: Convolutional networks for biomedical image segmentation. In *International Conference on Medical image computing and computer-assisted intervention*, pp. 234–241. Springer, 2015.

Rui, J., Wenbing, H., Yu, L., Deli, Z., and Yang, L. Space group constrained crystal generation. *arXiv:2402.03992*, 2024.

Saal, J. E., Kirklin, S., Aykol, M., Meredig, B., and Wolverton, C. Materials design and discovery with high-throughput density functional theory: the open quantum materials database (oqmd). *Jom*, 65(11):1501–1509, 2013.

Schmidt, J., Pettersson, L., Verdozzi, C., Botti, S., and Marques, M. A. L. Crystal graph attention networks for the prediction of stable materials. *Science Advances*, 7(49):eabi7948, 2021. doi: 10.1126/sciadv.abi7948. URL <https://www.science.org/doi/abs/10.1126/sciadv.abi7948>.

Siron, M., Djafar, I., Ritchie, L., Du-Fayet, E., Rossello, A., Ramlaoui, A., von Werra, L., Wolf, T., and Duval, A. Lemat-bulkunique dataset, 2024. URL <https://huggingface.co/datasets/LeMaterial/LeMat-BulkUnique>.

Su, J., Lu, Y., Pan, S., Wen, B., and Liu, Y. Roformer: Enhanced transformer with rotary position embedding. *arXiv preprint arXiv:2104.09864*, 2021. URL <https://arxiv.org/abs/2104.09864>.

Sultanov, A., Crivello, J.-C., Rebafka, T., and Sokolovska, N. Data-driven score-based models for generating stable structures with adaptive crystal cells. *Journal of Chemical Information and Modeling*, 63(22):6986–6997, 2023.

Takahara, I., Shibata, K., and Mizoguchi, T. Generative inverse design of crystal structures via diffusion models with transformers. *arXiv preprint arXiv:2406.09263*, 2024.

Tian, X., Xiang, F., Octavian-Eugen, G., Regina, B., and Tommi, J. Crystal diffusion variational autoencoder for periodic material generation, 2022. URL <https://arxiv.org/abs/2110.06197>.

Vaswani, A., Shazeer, N., Parmar, N., Uszkoreit, J., Jones, L., Gomez, A. N., Kaiser, Ł., and Polosukhin, I. Attention is all you need. *Advances in neural information processing systems*, 30, 2017.

Xiao, H., Li, R., Shi, X., Chen, Y., Zhu, L., Chen, X., and Wang, L. An invertible, invariant crystal representation for inverse design of solid-state materials using generative deep learning. *Nature Communications*, 14(1):7027, 2023.

Xiaoshan, L., Zhenyu, W., Pengyue, G., Jian, L., Yanchao, W., Changfeng, C., and Yanming, M. Deep learning generative model for crystal structure prediction, 2024. URL <https://arxiv.org/abs/2403.10846>.

Yang, M., Ma, M. Q., Li, D., Tsai, Y.-H. H., and Salakhutdinov, R. Complex transformer: A framework for modeling complex-valued sequence. *ArXiv*, abs/1910.10202, 2019. URL <https://arxiv.org/abs/1910.10202>.

Ye, C.-Y., Weng, H.-M., and Wu, Q.-S. Con-cdvae: A method for the conditional generation of crystal structures. *Computational Materials Today*, pp. 100003, 2024.

Yi, X., Xu, G., Xiao, X., Zhang, Z., Liu, L., Bian, Y., and Zhao, P. Crystaldit: A diffusion transformer for crystal generation. *arXiv preprint arXiv:2508.16614*, 2025.

Zeni, C., Pinsler, R., Zügner, D., Fowler, A., Horton, M., Fu, X., Wang, Z., Shysheya, A., Crabbé, J., Ueda, S., et al. A generative model for inorganic materials design. *Nature*, 639(8055):624–632, 2025.

Zhendong, C., Xiaoshan, L., Jian, L., and Lei, W. Space group informed transformer for crystalline materials generation. *arXiv:2403.15734*, 2024.

Zhu, R., Nong, W., Yamazaki, S., and Hippalgaonkar, K. Wycryst: Wyckoff inorganic crystal generator framework. *Matter*, 7(10):3469–3488, 2024.

5,005,017 unique crystal structures as determined by a fingerprinting procedure developed by the LeMaterial team. All structures in this subset were computed using the Perdew–Burke–Ernzerhof (PBE) exchange–correlation functional (Perdew et al., 1996), which remains the most commonly used functional for large public crystal databases due to its favorable trade-off between accuracy and computational efficiency. We refer to this dataset hereafter as *LeMat-BulkUnique-PBE*.

Pre-filters and splits We apply a sequence of standard pre-filters to *LeMat-BulkUnique-PBE* in order to obtain a clean and harmonized corpus suitable for large-scale pre-training. Specifically, we remove structures containing noble gases or *f*-block elements, structures with interatomic distances smaller than 0.5 Å, and duplicate structures identified using the `StructureMatcher` from PYMATGEN, with fractional length tolerance `ltol` = 0.2, site tolerance `stol` = 0.3, and angular tolerance `angle-tol` = 5°. These tolerance values follow commonly used defaults in prior work and are intended to remove only near-identical duplicates.

After filtering, the resulting dataset contains 2,838,937 structures and is publicly released in CIF format on HuggingFace¹. We refer to this corpus as the *LeMat-pretrain* dataset.

From *LeMat-pretrain*, we further extract a subset of at least metastable structures, defined as having an energy above the convex hull less than or equal to 0.1 eV/atom. Energies above hull are obtained from the *LeMat-Bulk-DFT-Hull-All* dataset², using the provided `dft-hull` values. This metastable subset contains 506,853 structures and is referred to as *LeMat-metastable*.

Train–test split From the metastable subset, we reserve 2,048 structures for testing. To ensure coverage across structural complexity, the test set is stratified by unit-cell size: 512 structures with ≤ 16 atoms, 512 with 17–32 atoms, 512 with 33–48 atoms, and 512 with 49–64 atoms. The remaining 504,805 metastable structures are used for training.

Appendix Overview

This appendix provides additional technical details, derivations, and extended experimental results that support the main text. The material is organized to mirror the structure of the paper and to facilitate reproducibility without interrupting the narrative flow of the main body.

A. Dataset and Preprocessing Details

A.1. Source datasets and harmonization

LeMaterial The *LeMaterial initiative* (LeMaterial Consortium, 2025) is a recent effort aimed at curating large-scale, high-quality open datasets and developing tooling to support machine-learning research in materials science. Its first major release, *LeMat-Bulk*, aggregates crystal structures computed using density functional theory (DFT) from three widely used public databases: the Materials Project (Jain et al., 2013), Alexandria (Schmidt et al., 2021), and the Open Quantum Materials Database (OQMD) (Saal et al., 2013).

In this work, we use the PBE subset of the *LeMat-BulkUnique* dataset (Siron et al., 2024), which contains

Fractional atomic coordinates are snapped to a rational grid defined by an integer denominator, such as 24 or 48. This discretization facilitates stable Fourier representations while preserving crystallographic symmetries. In fractional coordinates, the admissible translational components that can combine with integer rotation matrices to form lattice isomorphisms are drawn from the finite set $\{0, \frac{1}{6}, \frac{1}{4}, \frac{1}{3}, \frac{1}{2}\}$ (Aroyo, 2017). By choosing a snapping denominator that

¹https://huggingface.co/datasets/materials_toolkits/lematerial

²<https://huggingface.co/datasets/LeMaterial/LeMat-Bulk-DFT-Hull-All>

is a multiple of 12, all such symmetry-compatible translations arrive at the same rounding error on the snapping grid. As a result, symmetry-equivalent atoms are rounded coherently, ensuring that snapping does not break crystallographic equivalence relations.

In this work, 48 is the largest snapping denominator used, corresponding to a maximum roundoff error of 1/96, i.e. approximately 1% in fractional coordinates. This bound provides a lightweight justification that the induced quantization error remains small relative to typical structural variations while enabling exact recovery on the chosen grid.

A.3. Recoverability criteria and rejection conditions

The fractional-coordinate recovery procedure is described in detail in Appendix G. In brief, recovery is attempted in a sequence of up to three stages of increasing numerical precision and computational cost. If recovery fails at a given stage, the procedure advances to the next stage.

Because fractional coordinates are snapped to a rational grid, we require exact recovery of all fractional coordinates for all atomic species present. Crystals for which exact recovery fails after the final stage are rejected. This criterion is applied prior to training and ensures that Fourier coefficients can be mapped unambiguously back to fractional coordinates, allowing reconstruction accuracy to be assessed without storing explicit coordinates alongside the Fourier representation.

B. Representation and Symmetry Structure

B.1. Rotation-invariant lattice parameterization

Material properties derived from a crystalline structure are invariant under global rotations of the crystallographic axes. Accordingly, we adopt a lattice representation that factors out rotational degrees of freedom while remaining well conditioned across a wide range of length scales.

Let $\mathbf{L} \in \mathbb{R}^{3 \times 3}$ denote the lattice matrix. We obtain a rotation-invariant encoding via the polar decomposition,

$$\mathbf{L} = \mathbf{R} \exp(\mathbf{S}),$$

where $\mathbf{R} \in \text{SO}(3)$ is a rotation and $\exp(\mathbf{S}) \in \text{Sym}^+(3)$ is symmetric positive definite. Equivalently, writing the singular value decomposition $\mathbf{L} = \mathbf{U} \mathbf{\Sigma} \mathbf{V}^\top$ with $\mathbf{\Sigma} = \text{diag}(\boldsymbol{\sigma})$, the polar factors are given by

$$\mathbf{R} = \mathbf{U} \mathbf{V}^\top, \quad \mathbf{S} = \mathbf{V} \text{diag}(\log \boldsymbol{\sigma}) \mathbf{V}^\top.$$

The matrix \mathbf{S} provides an additive, rotation-invariant parameterization of lattice geometry via the matrix logarithm of the symmetric polar factor, a construction that is standard in lattice analysis and geometry processing (). Isotropic

rescaling corresponds to shifts proportional to the identity, while anisotropic deformations are encoded by traceless components. This parameterization is therefore well suited for learning and optimization across diverse lattice scales.

B.2. Choice of truncation geometry

The truncated Fourier representation requires selecting a finite subset of reciprocal-space wave vectors \mathcal{J} . While spherical truncation ($\|\mathbf{j}\|_2 \leq j_{\max}$) is analytically natural for isolated atoms or radially symmetric densities, we find it poorly matched to crystalline configurations, which often exhibit separable structure along lattice-aligned directions.

Across a large and diverse corpus of crystalline materials, cubic truncation ($\|\mathbf{j}\|_\infty \leq j_{\max}$) consistently yields higher reconstruction success rates than spherical or hybrid truncation schemes, even in cases where the latter retain a larger number of Fourier modes. We therefore adopt cubic truncation throughout this work as a practical and empirically robust choice.

Reconstruction limits under cubic truncation Using cubic truncation, reconstruction success varies smoothly with atomic count and unit-cell occupancy. For 7^3 retained modes ($j_{\max} = 3$), we observe at least one crystal containing 52 atoms of a single species that can be fully reconstructed from its truncated Fourier representation. Increasing the resolution to 9^3 modes ($j_{\max} = 4$) similarly permits reconstruction of at least one crystal containing 108 atoms of a single species. These observations illustrate the scaling behavior of recoverability under cubic truncation and motivate the use of higher Fourier resolution when targeting structurally complex or high-occupancy unit cells.

B.3. Fourier-space symmetries and algebraic constraints

Crystallographic symmetries act on atomic configurations as isomorphisms generated by compositions of rotations and translations that preserve the lattice (Klipfel et al., 2023; Zeni et al., 2025). When expressed in fractional coordinates, admissible rotational symmetries are represented by integer-valued matrices $\mathbf{M} \in \mathbb{Z}^{3 \times 3}$ with $\det \mathbf{M} = \pm 1$, corresponding to lattice automorphisms. Associated symmetry translations $\boldsymbol{\delta} \in \mathbb{R}^3$ are restricted to rational fractional shifts consistent with the space group of the crystal.

Under such a symmetry operation, a fractional atomic coordinate $\mathbf{f} \in \mathcal{U}_z$ transforms as

$$\mathbf{f}' = \mathbf{M} \mathbf{f} + \boldsymbol{\delta} \pmod{1}.$$

Substituting this transformation into the definition of the truncated Fourier coefficients yields an induced action on reciprocal-space components. In particular, the Fourier coefficients for species z satisfy

$$\boldsymbol{\alpha}_j^{(z)} = \exp(-2\pi i \mathbf{j}^\top \boldsymbol{\delta}) \boldsymbol{\alpha}_{\mathbf{M}^\top \mathbf{j}}^{(z)},$$

where the rotation permutes wave vectors via $j \mapsto M^\top j$ and the translation contributes a phase factor.

These algebraic constraints encode crystallographic symmetry directly in reciprocal space, revealing structured redundancies among Fourier coefficients. In the proposed representation, such redundancies can be learned, compressed, and respected implicitly in the latent space, without requiring explicit symmetry enforcement during generation.

C. Tokenization and Embedding Details

This section specifies the tokenization and embedding scheme summarized in the main text, describing how lattice geometry, species identity, and Fourier coefficients are embedded into a unified complex-valued token sequence.

C.1. Token construction and embedding

The transformer input consists of a small set of global descriptors together with a structured collection of complex Fourier coefficients representing the atomic density. All components are embedded into a common complex vector space $\mathbb{C}^{d_{\text{model}}}$ prior to transformer processing.

Global descriptors comprise the rotation-invariant lattice parameters described in Appendix B.1 and the identities of the atomic species present in the structure. Local structural information is represented by one token per retained reciprocal-space wave vector.

C.2. Species-slot assignment and randomization

The architecture supports up to six distinct atomic species per structure. This limit is dataset-driven and synthesis-practical, excluding fewer than 0.01% of structures while substantially simplifying token routing and improving compression efficiency.

Species identities are represented using learned embeddings without imposing explicit chemical priors. When a structure is drawn from the training set, the assignment of species to the six available slots is randomized: a nonzero column is selected uniformly at random, and remaining species are placed consecutively modulo six. This permutation is applied coherently across all Fourier rows so that each species occupies a single column throughout the representation. The procedure prevents systematic undertraining of specific slots while preserving species consistency across tokens.

C.3. Global structure token construction

For each structure, the six lattice parameters and the embeddings corresponding to the species present (ordered by atomic number, consistent with the Fourier representation) are concatenated into a single real-valued vector. This vec-

tor is mapped through a learned linear projection from $\mathbb{R}^{6(1+d_{\text{enc}})}$ to $2d_{\text{model}}$ real channels, which are interpreted as a complex vector in $\mathbb{C}^{d_{\text{model}}}$. The result is a single global token encoding lattice geometry and species composition.

C.4. Fourier token projection and parameterization

The truncated Fourier representation is organized as a matrix of complex coefficients, with rows indexed by reciprocal-space wave vectors and columns by species slots. Species absent from a structure have identically zero coefficients in the corresponding columns.

The Fourier rows, each represented as a vector in \mathbb{C}^6 , are also mapped to complex tokens, one per wave vector, by a complex-valued linear transformation. Using a single shared projection enforces consistent parameterization across reciprocal space. Because the input is already complex-valued, this projection halves the number of learnable parameters relative to an equivalent real-valued projection with doubled channel width, while preserving the total number of real-valued floating-point operations.

Auxiliary tokens and capacity control

A small block of auxiliary complex tokens with learned initial values is prepended to the token sequence. These tokens provide the depth-aligned scaffold that becomes the auxiliary ladder encoding. The number of auxiliary tokens is treated as a hyperparameter and is chosen in proportion to Fourier resolution (e.g., 5 auxiliary tokens for 7^3 retained modes and 9 for 9^3). Auxiliary tokens are initialized from trainable parameters and introduced once at the input.

D. Complex Transformer Blocks

Each layer of the encoder and decoder consists of a standard transformer block adapted to operate natively on complex-valued token representations. The overall structure follows a pre-norm normalization–attention–MLP pipeline with residual connections applied at each sublayer, using complex-valued linear maps and geometry-aware positional encoding.

D.1. Complex RMS normalization

Let $X \in \mathbb{C}^{S \times d_{\text{model}}}$ denote the input token sequence. We apply a complex-valued RMS normalization based on the mean squared modulus of the activations,

$$\hat{X} = \frac{X}{\sqrt{\mathbb{E}[|X|^2] + \varepsilon}},$$

where the expectation is taken over the feature dimension. This normalization is independent of the complex phase of the input and rescales each token uniformly. In practice, X is represented as a real tensor of dimension $2d_{\text{model}}$, and the mean of squared real components is computed, differing

from real RMS normalization by only a constant factor.

After normalization, a learned complex affine transformation is applied,

$$\text{RMSNorm}(X) = \hat{X} \odot w + b,$$

with complex-valued scale $w \in \mathbb{C}^{d_{\text{model}}}$ and bias $b \in \mathbb{C}^{d_{\text{model}}}$. Magnitude-based normalization in complex space is consistent with prior complex transformer designs (Yang et al., 2019; Eilers & Jiang, 2023). We include a complex bias term, which empirically improves VAE optimization (see ablation study).

D.2. Complex multi-head attention and real-valued kernels

Queries, keys, and values are produced via complex linear projections of the normalized activations,

$$Q = \hat{X}W_Q, \quad K = \hat{X}W_K, \quad V = \hat{X}W_V,$$

with $W_Q, W_K, W_V \in \mathbb{C}^{d_{\text{model}} \times d_{\text{model}}}$. These tensors are reshaped into multiple heads in the standard manner.

To ensure that attention weights form convex combinations of values, attention logits are computed from a real-valued similarity measure. Specifically, the attention score between a query q and key k is given by

$$\text{score}(q, k) = \Re(q^\top k^*).$$

In implementation, real and imaginary components are packed as additional feature dimensions and standard scaled dot-product attention (SDPA) kernels are applied to the resulting real-valued tensors. This yields real, properly normalized attention weights while preserving compatibility with optimized attention implementations.

D.3. Complex Fourier rotational positional encoding (RoPE3D)

Positional information is incorporated using a complex-valued rotational positional encoding (RoPE), extending the formulation of Su et al. (2021) to three-dimensional reciprocal space. Each attention head of dimension d_{head} is constructed such that d_{head} is divisible by three and is partitioned into equal subspaces corresponding to the x , y , and z components of a reciprocal-space wave vector.

For Fourier tokens, base rotation angles are deterministically derived from the associated wave vectors using a fixed set of geometrically scaled frequencies. Auxiliary and global tokens, which do not correspond to specific reciprocal-space locations, receive zero base angles. In all cases, trainable per-head and per-channel phase offsets are added, allowing the model to adapt the positional encoding during training.

The resulting rotations are applied elementwise to queries and keys via multiplication by $\exp(i\theta)$, where θ denotes the sum of base and learned angles. Because representations are complex-valued, positional encoding reduces to a simple complex phase rotation.

D.4. Complex gated MLP

Following the attention sublayer, a complex-valued gated MLP is applied. We consider two gating formulations that differ in how nonlinear modulation is applied to complex activations.

Separate real–imaginary gating (baseline) In the baseline architecture, activations are complex RMS-normalized and projected into two complex-valued streams, U and G , using complex linear maps. Gating is applied by interpreting these tensors in their real-valued representation: a SiLU nonlinearity is applied independently to the real and imaginary components of G , and the result is multiplied elementwise with the corresponding components of U . The gated output is then reassembled into a complex tensor and passed through a final complex linear projection. Optional dropout is applied to the update stream prior to gating.

This formulation provides flexible component-wise modulation but does not explicitly preserve phase structure under nonlinear gating.

Complex modulus gating (phase-preserving variant) In the modulus-gated variant, activations are complex RMS-normalized and projected into a single complex update stream U . A real-valued gate G is computed from the concatenated real and imaginary components of the normalized activations using a real linear projection followed by a SiLU nonlinearity. Dropout is applied independently to the real and imaginary parts of U prior to gating. The gated activation is then formed by modulating the complex update stream with the real-valued gate, $U \odot G$, and projected back to d_{model} .

Because the gate acts multiplicatively on the activation magnitude, this formulation modulates amplitude while preserving relative phase information across complex channels. As shown in the ablation study (Section 6.5), this variant reduces computational overhead and improves optimization efficiency relative to separate real–imaginary gating.

D.5. Residual composition

Attention and MLP sublayers are combined using standard pre-norm residual connections. Given an input X , the block computes

$$Y = X + \text{Attention}(\text{RMSNorm}(X)), \\ Z = Y + \text{MLP}(\text{RMSNorm}(Y)),$$

with all operations performed in complex space. This yields a direct complex-valued analogue of the standard transformer block (Vaswani et al., 2017), while preserving compatibility with efficient real-valued kernels where appropriate.

E. Auxiliary Ladder and Channel Suppression

This section describes the auxiliary ladder compression mechanism, including channel-wise masking, signal-to-noise regularization, and the nonzero-element (nnz) scheduling strategy used to suppress and prune latent channels during training.

E.1. Channel-wise masking and selector dynamics

The auxiliary ladder is formed by concatenating auxiliary token states extracted at each encoder depth, yielding a depth-aligned latent representation $\mu \in \mathbb{C}^{(Ln_{\text{aux}}) \times d_{\text{model}}}$. To encourage compression and enable adaptive channel pruning, we apply a learned real-valued mask of the same shape as the auxiliary ladder, with one scalar mask parameter per complex channel. Each mask element jointly scales the real and imaginary components of its associated channel, thereby modulating the channel magnitude.

Mask parameters are trained under a signal-to-noise regularization scheme that penalizes the ℓ_1 norm of the ratio between channel magnitudes and their corresponding learned noise scales. This formulation yields constant-magnitude gradients with respect to channel amplitude per unit noise, even as activations approach zero, preventing early gradient collapse and enabling principled suppression of non-informative channels. Adaptive, channel-specific noise scales were found to substantially improve optimization stability compared to a shared noise level.

Channels whose masked magnitudes are driven sufficiently close to zero are eligible for permanent removal through the nnz scheduling mechanism described below, producing a binary selector that deactivates pruned channels.

E.2. Latent signal-to-noise regularization

Latent regularization is implemented directly on the auxiliary ladder via an explicit signal-to-noise ratio (SNR) penalty, rather than through a Gaussian KL divergence. Given the auxiliary ladder mean μ and learned per-channel log-scale σ , the penalty is defined as

$$\mathcal{L}_\mu = \frac{1}{Ln_{\text{aux}} d_{\text{model}}} \sum \frac{|\mu|}{\exp(\sigma)}, \quad (4)$$

where $|\mu| = \sqrt{\Re(\mu)^2 + \Im(\mu)^2}$ denotes the complex modulus and the sum runs over all elements of the auxiliary ladder.

This SNR-based penalty maintains nonvanishing gradient pressure in the low-amplitude regime, in contrast to Gaussian KL regularization whose gradient vanishes near zero. As a result, it promotes learned channel suppression and provides a continuous signal that complements the discrete pruning induced by masking and nnz scheduling.

E.3. Nonzero-element scheduling and pruning

In addition to continuous suppression, we employ an explicit nonzero-element (nnz) scheduling mechanism to permanently prune latent channels. Here, a *channel* refers to a single complex element of a single auxiliary token; channels are not shared across tokens or depths.

Training begins with all auxiliary ladder channels active. Over a prescribed number of steps, the target nnz count is annealed from the full channel set to a final value using a cosine schedule. At each pruning step, channels are ranked by the magnitude of their learned mask values, and the lowest-ranked channels are irreversibly dropped to meet the current nnz target. Dropped channels are permanently deactivated and do not re-enter training.

The final nnz target and the duration of the cosine schedule are treated as hyperparameters and are varied in the extended sensitivity experiments reported in Appendix I.1. This combination of continuous suppression and scheduled pruning enables efficient capacity allocation while maintaining stable optimization.

F. Training Objectives and Optimization

F.1. Scale-Invariant Reconstruction Loss

Direct summation of reconstruction losses yields gradients proportional to absolute error magnitude, causing optimization pressure to decay rapidly as reconstruction improves. To maintain stable and balanced gradients throughout training, lattice and Fourier reconstruction losses are combined using an ℓ_2 aggregation,

$$\mathcal{L}_{\text{rec}} = \sqrt{\mathcal{L}_{\text{lat}} + \mathcal{L}_{\text{four}}}. \quad (5)$$

This corresponds to an ℓ_2 norm over stacked reconstruction residuals and yields gradients that are normalized in direction and weakly dependent on overall error scale. As a result, the relative weighting between lattice and Fourier reconstruction remains stable across training, without requiring manual rebalancing.

F.2. Latent regularization and relation to KL divergence

Latent regularization is implemented using the signal-to-noise-based penalty defined in Appendix E.2, rather than a Gaussian KL divergence. This choice is motivated by optimization behavior rather than a departure from the vari-

ational framework.

Under a diagonal complex Gaussian posterior with mean μ and variance $\exp(2\sigma)$, the KL divergence to a zero-mean prior with matched variance is proportional to the squared normalized mean,

$$\text{KL} \propto \sum |\mu|^2 / \exp(2\sigma).$$

The SNR penalty replaces this quadratic dependence with a monotonic function of the same quantity,

$$\sum |\mu| / \exp(\sigma),$$

which preserves the ordering induced by KL divergence while maintaining approximately constant gradient pressure as channel amplitudes approach zero.

From an information-theoretic perspective, this can be viewed as optimizing a monotonic surrogate of the KL divergence that emphasizes suppressibility and channel selection over strict moment matching. This modification avoids the vanishing gradients of Gaussian KL regularization in the low-amplitude regime, enabling learned channel suppression and effective interaction with the masking and nnz pruning mechanisms described in Appendix E.

F.3. Optimization schedules and weight decay

All models are trained using Adam optimization. We use an initial learning rate of 2×10^{-4} , with linear warmup from 10^{-7} over the first 1,000 steps, followed by cosine decay to 2×10^{-5} over a single training epoch (approximately 3.3×10^5 steps). Light weight decay (10^{-9}) is applied during warmup only and disabled thereafter. No gradient clipping or mixed-precision training is used.

G. Multistage Reconstruction of Atomic Coordinates

After the final decoder block, linear reconstruction heads map the decoded global structure token to lattice parameters and species logits (one slot per species), and map the decoded Fourier tokens to species-resolved Fourier coefficients for each retained reciprocal-space wave vector. Fractional atomic coordinates are then recovered from the Fourier representation using a multistage procedure described below.

Reconstruction is performed independently for each atomic species. The number of atoms n_z of a given species is determined *a priori* from the zero-frequency Fourier coefficient $\alpha_{j=0}$. Recovery proceeds in three stages of increasing precision and computational cost. If reconstruction fails after the final stage, the structure is rejected.

G.1. Stage 1: Direct density-peak recovery

We evaluate the reconstructed atomic density on a discrete fractional-coordinate grid matching the rational grid used during preprocessing (e.g., 48^3 grid points for denominator 48),

$$\rho(\mathbf{f}) = \sum_{j \in \mathcal{J}} \alpha_j \exp(2\pi i \mathbf{j}^\top \mathbf{f}),$$

and select the n_z grid points with maximal density. When fractional coordinates have been pre-rounded to this grid, these maxima typically coincide with the original rounded coordinates. The majority of structures are fully recovered at this stage.

G.2. Stage 2: Iterative atom removal

If direct density-peak recovery fails to identify all atoms, coordinates are recovered sequentially using a greedy procedure. After identifying a density maximum at \mathbf{f}_a , its exact Fourier contribution,

$$\exp(-2\pi i \mathbf{j}^\top \mathbf{f}_a),$$

is subtracted from the Fourier coefficients, assuming unit occupancy. The updated density is then recomputed and the next maximum located. This procedure is repeated until all n_z atoms are recovered or no further maxima can be identified. In practice, this stage resolves nearly all remaining cases.

G.3. Stage 3: Newton refinement and least-squares correction

In rare cases, nearby atoms may shift density maxima or lead to coincident grid locations. To resolve such ambiguities, we introduce a small random perturbation to all recovered coordinates and jointly refine the full set of atomic positions for a given species by minimizing the residual between the target Fourier coefficients and those induced by the reconstructed coordinates.

Let $\mathcal{U} = \{\mathbf{f}_a\}$ denote the current set of fractional coordinates for a species, and let $\mathcal{F}(\mathcal{U})$ denote the corresponding truncated Fourier coefficients,

$$\mathcal{F}_j(\mathcal{U}) = \sum_{\mathbf{f}_a \in \mathcal{U}} \exp(-2\pi i \mathbf{j}^\top \mathbf{f}_a).$$

The partial derivatives with respect to each coordinate are

$$\frac{\partial \mathcal{F}_j}{\partial \mathbf{f}_a} = -2\pi i \mathbf{j} \exp(-2\pi i \mathbf{j}^\top \mathbf{f}_a),$$

which form a Jacobian matrix \mathbf{D} with columns corresponding to the flattened fractional coordinates in \mathcal{U} .

To maintain real-valued coordinates, we construct an augmented real system,

$$\begin{bmatrix} \Re(\mathcal{F}(\mathcal{U} + \Delta)) \\ \Im(\mathcal{F}(\mathcal{U} + \Delta)) \end{bmatrix} \approx \begin{bmatrix} \Re(\mathcal{F}(\mathcal{U})) \\ \Im(\mathcal{F}(\mathcal{U})) \end{bmatrix} + \begin{bmatrix} \Re(\mathbf{D}) \\ \Im(\mathbf{D}) \end{bmatrix} \Delta,$$

and solve the resulting least-squares problem using a standard SVD-based pseudoinverse,

$$\Delta = \mathbf{D}^\dagger [\mathcal{F}(\mathcal{U}) - \alpha].$$

Coordinates are updated as $\mathcal{U} \leftarrow \mathcal{U} - \Delta$ and the procedure is iterated up to a maximum of 10 iterations. If convergence is not achieved within this limit, reconstruction is deemed to have failed and the structure is rejected.

Crystallographic symmetry is handled implicitly through the Fourier representation: symmetry-related atoms induce identical constraints in reciprocal space, and no explicit symmetry enforcement is required during reconstruction.

H. Reverse Diffusion Formulation

This section describes the reverse diffusion formulation used to generate latent auxiliary ladders, including the noise model, information-matched diffusion schedule, and the lightweight conditioning mechanism used to modulate model parameters as a function of the diffusion coordinate.

H.1. Reverse diffusion noise model

Let $\mu \in \mathbb{C}^{T \times D}$ denote the latent auxiliary ladder, where T indexes auxiliary tokens (including depth) and D indexes complex channels. Each (t, d) entry is treated as an independent complex random variable with a shared noise scale across its real and imaginary components.

Diffusion noise is sampled from an isotropic radial Laplace distribution on $\mathbb{C} \simeq \mathbb{R}^2$,

$$p(\eta_{t,d}) \propto \exp\left(-\frac{|\eta_{t,d}|}{\tau_{t,d}}\right), \quad (6)$$

where $\tau_{t,d} > 0$ is a per-channel scale parameter. The radial component follows a Gamma distribution with shape $k = 2$ and scale $\tau_{t,d}$, yielding

$$\mathbb{E}[|\eta_{t,d}|] = 2\tau_{t,d}, \quad \mathbb{E}[|\eta_{t,d}|^2] = 6\tau_{t,d}^2.$$

During training, $\tau_{t,d}$ is estimated as a running average of the latent channel magnitudes,

$$\tau_{t,d} \leftarrow \frac{1}{2} \mathbb{E}[|\mu_{t,d}|], \quad (7)$$

where the expectation is taken over all training samples. This estimate is computed without gradient tracking, accumulated over a single training epoch, and then frozen. The resulting per-channel noise scales are used during sampling and reverse diffusion, but do not participate in VAE training.

H.2. Gaussian moment matching and variance calibration

To relate the Laplace noise model to standard diffusion formulations, we approximate each complex channel by an isotropic Gaussian with matched second moment. For a radial Laplace distribution in two dimensions with scale τ , the expected squared norm is $\mathbb{E}[|\eta|^2] = 6\tau^2$. Matching this to a complex Gaussian with variance ω^2 per real component yields

$$\mathbb{E}[|\eta|^2] = 2\omega^2 \Rightarrow \omega^2 = 3\tau^2. \quad (8)$$

This moment-matched Gaussian approximation is used solely to calibrate the diffusion schedule and does not alter the underlying Laplace noise model used during sampling.

H.3. Information-matched diffusion schedule

A scalar diffusion coordinate $\phi \in [\phi_{\min}, \phi_{\max}] \subset (0, 1)$ is sampled uniformly and shared across the batch. Sharing ϕ is a memory optimization that substantially reduces activation overhead while still covering the full diffusion trajectory over training.

The forward diffusion process is defined as

$$\mu_\phi = c_\phi \mu + s_\phi \eta, \quad c_\phi^2 + s_\phi^2 = 1, \quad (9)$$

where η is drawn from the Laplace distribution above. To define an information-aware schedule, we analyze the process under the Gaussian approximation from Appendix H.2.

Let $\exp(\sigma)$ denote the learned decoder noise scale associated with each latent channel. Under the Gaussian approximation, the effective signal-to-noise ratio is

$$R = \frac{\omega^2}{\exp(2\sigma)} = 3 \left(\frac{\tau}{\exp(\sigma)} \right)^2. \quad (10)$$

We choose mixing coefficients

$$s_\phi^2 = \frac{(1+R)^\phi - 1}{R}, \quad c_\phi^2 = 1 - s_\phi^2, \quad (11)$$

so that the expected information gained when moving from pure noise ($\phi = 1$) to an intermediate state μ_ϕ is approximately proportional to $1 - \phi$. In particular, $\phi = 0$ corresponds to the pure signal distribution, while $\phi = 1$ corresponds to the maximally corrupted prior. This yields a diffusion schedule in which ϕ is approximately linear in remaining information content.

H.4. Quadratic conditioning on diffusion coordinate

Several model components are conditioned on the diffusion coordinate ϕ using a lightweight quadratic interpolation scheme. For any parameter tensor Θ to be conditioned,

three control tensors $\{\Theta^{(0)}, \Theta^{(1)}, \Theta^{(2)}\}$ are learned, corresponding to $\phi = 0$, $\phi = \frac{1}{2}$, and $\phi = 1$. The interpolated parameter is given by

$$\Theta(\phi) = B_0(\phi) \Theta^{(0)} + B_1(\phi) \Theta^{(1)} + B_2(\phi) \Theta^{(2)},$$

with basis functions $B_0 = 2(0.5 - \phi)(1 - \phi)$, $B_1 = 4\phi(1 - \phi)$, and $B_2 = 2\phi(\phi - 0.5)$. This scheme provides smooth, degree-2 modulation of parameters as a function of ϕ without introducing additional networks or conditioning paths.

In practice, quadratic conditioning is applied to additive biases in complex RMS normalization, post-gating MLP biases, learned RoPE3D phase offsets, and per-head output scaling after attention.

I. Additional Experimental Results

I.1. Extended compression sweep results

This subsection reports robustness checks for auxiliary-ladder compression hyperparameters, including the target nonzero-element (nnz) budget and the compression schedule length. Results for the compression-strength sweep and the schedule-length sweep are reported in Tables 7 and 8, respectively.

Table 7 varies the target nnz factor C while holding the nnz schedule length fixed at 160k steps. Moderate compression achieves the best overall reconstruction quality, as reflected by the lowest total VAE loss and balanced lattice and Fourier reconstruction errors. More aggressive compression reduces latent magnitude but degrades reconstruction, while weaker compression yields no additional benefit.

Table 8 varies the length of the cosine nnz schedule for a fixed target compression factor $C = 8/12$. Performance varies smoothly with schedule length, with an intermediate schedule providing the best trade-off between reconstruction accuracy and latent suppression. Across both sweeps, the full VAE objective \mathcal{L}_{VAE} serves as the primary selection criterion, as it jointly accounts for lattice reconstruction, Fourier reconstruction, species prediction, and latent regularization.

Table 7. Compression strength sweep (vary target nnz factor C ; baseline nnz schedule length 160k steps). “C factor” sets the final target nnz as $6(1 + n_{\text{elements}} + \text{bpd}^3) C$. Best (lowest) values per column are bolded.

C factor	\mathcal{L}_{VAE}	$\mathcal{L}_{\text{four}}$	\mathcal{L}_{lat}	\mathcal{L}_{μ}	\mathcal{L}_{CE}
7/12	0.268	0.235	0.073	0.034	<0.001
8/12	0.221	0.209	0.034	0.043	0.001
9/12	0.254	0.223	0.068	0.041	0.001

Table 8. Compression schedule length sweep (vary “nnz steps”; baseline target nnz factor $C = 8/12$). “nnz steps” is the number of optimization steps over which the cosine schedule reaches the final nnz target. Best (lowest) values per column are bolded.

nnz steps	\mathcal{L}_{VAE}	$\mathcal{L}_{\text{four}}$	\mathcal{L}_{lat}	\mathcal{L}_{μ}	\mathcal{L}_{CE}
120k	0.241	0.205	0.071	0.036	0.003
160k	0.221	0.209	0.034	0.043	0.001
200k	0.230	0.198	0.068	0.040	0.001

Table 9. Meta-stable fine-tuning LR sweep (Baseline model). All values are RMSE. “low- ϕ ” corresponds to $\phi \in [0.01, 0.2]$.

lr	low- ϕ noise	mean noise	low- ϕ sig.
5×10^{-5}	5.464	3.027	0.634
2×10^{-5}	5.419	3.018	0.633
1×10^{-5}	5.417	3.025	0.635
5×10^{-6}	5.427	3.035	0.636
2×10^{-6}	5.452	3.052	0.639

I.2. Reverse diffusion fine-tuning robustness

This subsection reports robustness checks for reverse diffusion fine-tuning across a sweep of learning rates, evaluated for both the baseline architecture and a variant with $N_{\text{head}} = 10$. Results are summarized in Tables 9 and 10, respectively.

Metrics follow the main text: noise RMSE in the signal-dominant regime (low- ϕ), mean noise RMSE across the diffusion trajectory, and one-shot signal reconstruction RMSE in the signal-dominant regime (diagnostic). The low- ϕ bin corresponds to $\phi \in [0.01, 0.2]$, where inputs are largely signal-dominated and denoising is most challenging.

Across both architectures, performance varies smoothly over more than an order of magnitude in learning rate, with no sharp instabilities observed. The $N_{\text{head}} = 10$ architecture consistently achieves lower noise RMSE than the baseline, both in the signal-dominant regime and on average across the diffusion schedule. In all cases, signal reconstruction error in the low- ϕ regime remains below the decoder noise scale, indicating that reconstructed signals stay within the operating range of the decoder.

J. Limitations

Our approach relies on truncated Fourier representations and rational-grid snapping, which introduce controlled discretization error and impose resolution-dependent recoverability limits. Increasing Fourier resolution improves fidelity but incurs additional computational cost.

Coordinate recovery from Fourier coefficients is performed via a multistage, non-differentiable procedure. While this decouples training from decoding, it may limit robustness

Table 10. Meta-stable fine-tuning LR sweep ($N_{\text{head}} = 10$ model). All values are RMSE. “low- ϕ ” corresponds to $\phi \in [0.01, 0.2]$.

lr	low- ϕ noise	mean noise	low- ϕ sig.
5×10^{-5}	4.700	2.665	0.604
2×10^{-5}	4.674	2.661	0.604
1×10^{-5}	4.675	2.666	0.605
5×10^{-6}	4.683	2.674	0.607
2×10^{-6}	4.702	2.686	0.609

for extremely dense unit cells.

Finally, unconditional latent diffusion is observed to amplify dataset skew toward the small-cell regime. Although this does not affect reconstruction or denoising capability, it limits unconditional generation diversity and motivates future work on conditional generation, size-aware priors, or guided diffusion.